The Astrophysical Journal, 708:625–634, 2010 January 1 doi:10.1088/0004-637X/708/1/625

THE MASS OF THE CANDIDATE EXOPLANET COMPANION TO HD 136118 FROM *HUBBLE SPACE TELESCOPE* ASTROMETRY AND HIGH-PRECISION RADIAL VELOCITIES*

Eder Martioli[1], Barbara E. McArthur[2], G. Fritz Benedict[2], Jacob L. Bean[3], Thomas E. Harrison[4,5], and Amber Armstrong[2]

[1] Divisão de Astrofísica, Instituto Nacional de Pesquisas Espaciais, S. J. dos Campos, SP, Brazil; edermartioli@gmail.com
[2] Department of Astronomy, University of Texas at Austin, RLM 15.202AA, Austin, TX 78712, USA
[3] Institut für Astrophysik, Georg-August-Universität Göttingen, Friedrich-Hund-Platz 1, 37077 Göttingen, Germany
[4] Astronomy Department, New Mexico State University, P.O. Box 30001, MSC 4500, Las Cruces, NM, 88003, USA
Received 2009 August 21; accepted 2009 November 16; published 2009 December 14

ABSTRACT

We use *Hubble Space Telescope* fine guidance sensor astrometry and high-cadence radial velocities for HD 136118 from the Hobby–Eberly Telescope with archival data from Lick to determine the complete set of orbital parameters for HD 136118 b. We find an orbital inclination for the candidate exoplanet of $i_b = 163.^{\circ}1 \pm 3.^{\circ}0$. This establishes the actual mass of the object, $M_b = 42^{+11}_{-18}\ M_J$, in contrast to the minimum mass determined from the radial velocity data only, $M_b \sin i \sim 12\ M_J$. Therefore, the low-mass companion to HD 136118 is now identified as a likely brown dwarf residing in the "brown dwarf desert."

Key words: astrometry – planetary systems – stars: individual (HD136118) – stars: low-mass, brown dwarfs – techniques: radial velocities

Online-only material: color figure

1. INTRODUCTION

Among the hundreds of exoplanets detected so far, only a few of them have their actual mass known. The widely used Doppler spectroscopy technique yields the radial component of the stellar perturbation velocity only. Consequently, the inclination of the orbital plane is unknown and only the minimum mass of a companion may be determined. To obtain a companion's true mass it is necessary to make use of additional techniques.

The first precise determination of an exoplanet mass was made for a transiting system (Henry et al. 2000). However, transits are observed to occur only for systems that are oriented edge-on, and they have only a reasonable probability of occurrence for close-in planets (semimajor axes less than about 0.1 AU). Another way to determine the orbital inclination of an unseen companion is by measuring the stellar reflex motion astrometrically. The first astrometrically determined mass of an exoplanet by Benedict et al. (2002b) was possible, thanks to the high precision of the fine guidance sensor (FGS) instrument on the *Hubble Space Telescope* (*HST*). The FGS provides per observation precisions of better than 1 mas for small angle relative astrometry. This unique capability enables the detection of stellar perturbations due to planetary mass companions in wide orbits.

We were granted observing time with the *HST* to measure the perturbation and determine the true mass of HD 136118 b, which is an exoplanet candidate found by radial velocity (RV) measurements (Fischer et al. 2002). To supplement previously published data and provide better constraint on the companion's spectroscopic orbital parameters, we also obtained high-cadence RV measurements with the Hobby–Eberly Telescope (HET). In this paper, we present the results of our analysis, arranged as follows. In Section 2, we review stellar properties for HD 136118. In Section 3, we discuss the instrumental set-up and data reduction for both spectroscopy and astrometry. In Section 4, we describe the orbital model used to analyze this data. In Section 5, we discuss the strategy employed to obtain the system parameters, and present our results. In Section 6, we summarize and discuss the consequences of our results.

2. STELLAR PROPERTIES

HD 136118 (=HIP 74948) is a $V = 6.93$, F9 V star with roughly solar photospheric abundances (Gonzalez & Laws 2007). Table 1 summarizes its observed properties given in the literature. Observations of Ca II H and K lines (Fischer et al. 2002) indicate modest chromospheric activity for this star, therefore not many spots should be expected. Using the Saar & Donahue (1997) relationship for the spot RV amplitude versus filling factor, $A_S = 6.5 f_S^{0.9} v \sin i$, where f_S is spot filling factor in percent, $v \sin i$ is the projected velocity in km s^{-1}, and A_S is the spot RV amplitude in m s^{-1}. For the RV amplitude of 211 m s^{-1}, and the measured velocity $v \sin i = 7 \pm 0.5$ km s^{-1} (Butler et al. 2006), we obtain a spot filling factor of about 6%, i.e., about 60 milimag variations. As shown in Benedict et al. (1998) and Nelan et al. (2007), the FGS itself is a millimag precision photometer. The variations we see in HD 136118 over 700 days are on order 4 parts per 1000, about 4 millimag, as shown in Figure 1. This implies only small variations in spectral line shapes, which typically introduces noise on the order of 5–10 m s^{-1} in the velocities.

Fischer et al. (2002) have also provided evidence that the stellar rotation period is about 12.2 days. Given a stellar

* Based on observations made with the NASA/ESA *Hubble Space Telescope*, obtained at the Space Telescope Science Institute, which is operated by the Association of Universities for Research in Astronomy, Inc., under NASA contract NAS5-26555. Based on observations obtained with the Hobby–Eberly Telescope, which is a joint project of the University of Texas at Austin, the Pennsylvania State University, Stanford University, Ludwig-Maximilians-Universitt München, and Georg-August-Universität Göttingen.

[5] Visiting Astronomer, Kitt Peak National Observatory, National Optical Astronomy Observatory, which is operated by the Association of Universities for Research in Astronomy, Inc., under cooperative agreement with the National Science Foundation.

Table 1
Properties of HD 136118

ID	HD 136118	Unit	Reference
R.A.(2000)	15:18:55.4719 (8.18)	h:m:s	a
Decl.(2000)	−01:35:32.590 (5.37)	d:m:s	a
μ_α	−124.1 (0.9)	mas yr^{-1}	h
μ_δ	23.5 (0.7)	mas yr^{-1}	h
$\pi_{\rm abs}$	19.1 (0.8)	mas	h
Γ	−3.6 (0.1)	km s^{-1}	a
Spc type	F9V	...	h
Age	4.8 ($^{+0.7}_{-1.9}$)	Gyr	e
[Fe/H]	−0.010 (0.053)	dex	g
[C/H]	0.049 (0.081)	dex	g
[O/H]	0.112 (0.045)	dex	g
[Si/H]	−0.042 (0.058)	dex	g
[Ca/H]	−0.057 (0.062)	dex	g
d	52.3 (0.6)	pc	h
$v \sin i$	7.33 (0.5)	m s^{-1}	f
$P_{\rm rot}$	12.2	day	c
$T_{\rm eff}$	6097 (44)	K	f
$\log g$	4.16 (0.09)	cm s^{-2}	b
M_*	1.24 (0.07)	$M_\odot$	c
R_*	1.58 (0.11)	$R_\odot$	b
BC	0.01 (0.03)	mag	b
M_V	3.34	mag	d
B	7.432	mag	d
V	6.945	mag	d
R	6.630	mag	d
J	5.934	mag	d
H	5.693	mag	d

Notes.
[a] Perryman (1997).
[b] Allende Prieto & Lambert (1999).
[c] Fischer et al. (2002).
[d] Zacharias et al. (2004).
[e] Age value and limits derived from isochrone method (Saffe et al. 2005).
[f] Butler et al. 2006.
[g] Gonzalez & Laws (2007).
[h] This paper.

radius of $R = 1.58 \pm 0.11\,R_\odot$ (Allende Prieto & Lambert 1999), we calculate the maximum rotation speed at the stellar equator $v_{\rm max} = 6.5 \pm 0.2$ km s^{-1}. The measured projected velocity $v \sin i = 7 \pm 0.5$ km s^{-1} is then consistent with the maximum speed. This suggests a very high inclination of the spin axis. Therefore, if the whole system follows the same angular momentum orientation as that of the star, then the companion's orbit would be close to an edge-on orientation with respect to our line of sight.

3. OBSERVATIONS AND DATA REDUCTION

3.1. HET Spectroscopy Data

Spectroscopic observations were carried out with the High Resolution Spectrograph (HRS; Tull 1998) on the HET at the McDonald Observatory using the iodine absorption cell method (Butler et al. 1996). Our observations include a total of 168 high-resolution spectra which were obtained between UT dates 2005 December 4 and 2008 May 20. Multiple observations were taken most nights, so the velocities obtained on the same night were combined, producing individual measurements of the stellar RV at 61 different epochs.

The spectrograph was used in the $R = 60{,}000$ mode with a 316 line mm^{-1} echelle grating. The position of the cross

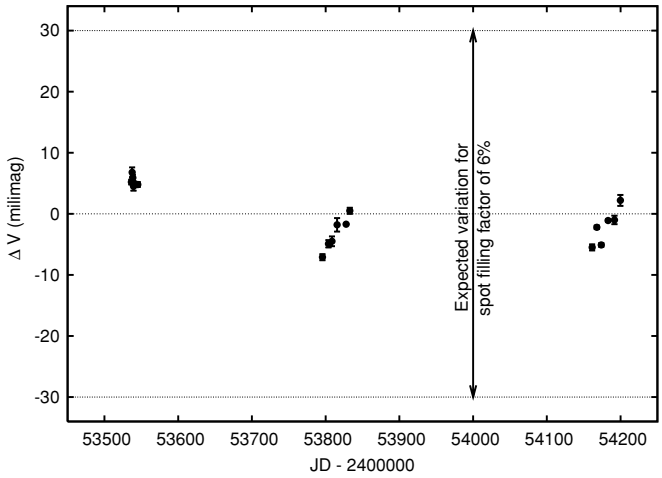

Figure 1. FGS-1r photometry of HD136118. Magnitude variation is relative to the mean magnitude, $V = 6.93$. Dashed lines show the amplitude of variation possible from a (single) spot filling factor of 6%, the spot filling factor required to produce the observed RV variation from HD136118 b (Saar & Donahue 1997).

dispersion grating was chosen so that the central wavelength of the order that fell in the break between the two CCD chips was 5936 Å. A temperature controlled cell containing low pressure iodine (I_2) gas was placed in front of the spectrograph slit entrance during all the exposures. The absorption of light by the I_2 gas produces a set of well-known spectral features imprinted at the same time as the stellar spectrum. However, they are produced with no wavelength shift with respect to the observatory frame. This provides a much better reference for wavelength calibration and also permits us to characterize the instrumental profile with great accuracy.

The exposure times were nominally 120 s, but were increased on a few nights due to bad seeing conditions. In addition to the program spectra we have also obtained HD 136118 template spectra. For these we removed the I_2 cell, the resolution was set to $R = 120{,}000$, and the exposure times were 230 s.

A detailed description of our reduction and RV analysis of HET HRS data is given in Bean et al. (2007). This provides us with measurements of the stellar RV relative to an arbitrary zero point obtained from individual spectra. The offset of the entire data set is determined simultaneously with the orbital fit, then, after compensating for this offset, we combined our RV data with previously published velocities from Lick Observatory (Fischer et al. 2002) to produce a total data set that spans 10.3 yr. Table 2 contains reduced HET data for the observed epochs.

3.2. HST Astrometry Data

Astrometric observations were obtained with the fine guidance sensor 1r (FGS-1r), a two-axis, white-light interferometer aboard *HST*. Our data were obtained with the FGS in fringe-tracking position mode. A detailed description of this instrument is found in Nelan et al. (2007). All observations were secured under 2-gyro guiding, an operational mode dictated by gyro failures on *HST*. This mode results in major constraints on *HST* roll angle and observation dates. The dates of observation, the number of measurements for each date ($N_{\rm obs}$), and the FGS-1r orientation angles are listed in Table 3. Our data sets span 1.8 yr, covering about 55% of the companion's orbital period.

In order to obtain high astrometric precision (∼1 mas) with FGS, we perform the following reduction procedures to remove the main sources of systematics. We apply an optical field angle

Table 2
HET Relative Radial Velocities for HD 136118

HJD−2450000	RV (m s^{-1})	± Error
3472.831	432.6	4.1
3482.881	421.4	3.5
3527.763	407.8	4.8
3544.727	392.4	4.1
3575.630	394.6	4.6
3755.051	319.0	10.6
3757.041	320.5	8.4
3765.026	312.2	8.8
3766.026	313.0	8.8
3767.020	321.9	7.7
3769.011	321.9	8.2
3787.982	329.2	7.5
3808.904	319.1	6.9
3809.909	322.5	7.8
3815.886	342.9	7.3
3816.898	334.4	7.3
3816.965	338.7	7.7
3818.873	324.5	8.0
3820.897	337.5	9.2
3832.840	331.2	6.9
3835.853	333.6	6.9
3836.858	334.6	10.2
3840.895	321.5	6.1
3844.909	328.9	5.6
3866.774	335.1	5.4
3867.754	332.1	4.3
3877.724	328.3	4.1
3880.810	339.0	5.0
3883.778	329.3	3.7
3888.700	330.7	4.2
3890.679	333.3	4.9
3891.682	333.7	4.6
3892.689	329.5	4.7
3893.768	325.2	4.4
3895.744	341.4	4.4
3897.749	332.9	4.6
3898.678	339.1	4.5
3901.740	336.0	4.3
3905.734	341.8	5.7
3911.730	333.9	5.8
3917.689	345.5	4.8
3938.639	341.2	16.4
3937.648	350.4	4.6
3939.631	338.5	4.7
4129.036	598.0	9.3
4131.023	587.5	9.0
4135.035	601.4	10.3
4144.998	619.0	8.0
4164.019	660.3	7.7
4176.992	696.4	7.3
4180.889	698.6	6.1
4186.887	711.6	5.5
4190.869	711.2	6.5
4191.864	713.7	5.9
4211.816	734.9	5.8
4221.789	744.9	5.7
4253.699	745.3	4.0
4282.631	735.8	4.9
4556.884	513.6	9.6
4565.914	510.6	8.7
4574.895	509.8	7.2
4580.893	491.0	7.2
4606.803	474.3	6.7

distortion (OFAD) calibration (Whipple et al. 1995; McArthur et al. 1997); apply time-dependent corrections to the OFAD (McArthur et al. 1997) with an additional, as yet unpublished, improvement due to additional up-to-date M35 data that has provided better models to recalibrate the telescope; and we correct for drift during each observation set (intra-orbit drift). These procedures are described in detail in Benedict et al. (1999, 2002a, 2002c) and McArthur et al. (2001).

Table 3
Log of Astrometric Observations

Epoch	Date	N_{obs}	*HST* Roll
1	2005 Jun 15	4	58.00
2	2005 Jun 16	4	58.00
3	2005 Jun 17	4	58.00
4	2005 Jun 18	4	58.00
5	2005 Jun 19	4	58.00
6	2005 Jun 24	4	59.10
7	2006 Mar 2	4	261.00
8	2006 Mar 10	4	264.17
9	2006 Mar 15	4	266.00
10	2006 Mar 22	4	269.15
11	2006 Apr 3	4	274.00
12	2006 Apr 7	4	280.41
13	2007 Mar 3	4	261.00
14	2007 Mar 9	4	263.67
15	2007 Mar 15	4	266.00
16	2007 Mar 24	4	269.74
17	2007 Apr 1	4	274.00
18	2007 Apr 8	4	280.70

Table 4
Classification Spectra and Photometric Information for HD136118 and the Astrometric Reference Stars

Star	Sp Ty	V	$B-V$	M_V	A_V
HD 136118	F9V	6.93	0.55	3.34	0.0
REF-14	K0V	13.95	0.86	5.88	0.12
REF-16	G0V	12.46	0.73	4.2	0.45
REF-17	K0.5III	13.55	1.13	0.65	0.21

The FGS provides the measurement of each star position in a serial fashion. Each date listed in Table 3 contains multiple measurements, alternating between the target (HD 136118) and the reference stars (REF-14, REF-16, and REF-17), comprising a total of about four measurements per star. This provides $x'(t)$ and $y'(t)$ coordinates at a time t of an epoch, which are in the *HST* reference frame.

A neutral density filter (F5ND) was applied when observing HD 136118 due to its brightness. For the reference stars we used the F583W filter.

3.3. Classification Spectra and Photometric Data

We obtained classification spectra data for the astrometric reference stars. We include this in the models as Bayesian a priori data to improve the accuracy of our determination of the orbital parameters for HD 136118 b. The spectra were obtained at the KPNO 4m Telescope and the photometric data at the NMSU 1m telescope in 2006 May. Table 4 summarizes spectral and photometric information for the reference stars.

3.4. Astrometric Model

Given the positions (x', y') measured by FGS-1r, we build a model that accounts for positional changes occurring systematically in all reference stars from date-to-date. This is accomplished by solving an overlapping plate model which includes scaling rotation (C_1, C_2, C_3, C_4) and offset (D_1, D_2)

Table 5
Astrometry Catalog

Star	R.A.[a] (deg)	Decl.[a] (deg)	ξ[b] (arcsec)	η[b] (arcsec)	μ_α(mas yr^{-1})	μ_δ(mas yr^{-1})	$\pi_{\rm abs}$(mas)	d (pc)
HD 136118	229.731	−1.592	59.8049 ± 0.0002	659.3195 ± 0.0002	−124.06 ± 0.15	23.48 ± 0.17	19.12 ± 0.23	52.3 ± 0.6
REF-14	229.739	−1.628	16.4201 ± 0.0001	783.7892 ± 0.0002	−7.39 ± 0.18	12.03 ± 0.23	2.75 ± 0.23	363 ± 30
REF-16	229.768	−1.591	−72.6629 ± 0.0001	638.4385 ± 0.0001	1.42 ± 0.13	−7.21 ± 0.14	2.73 ± 0.18	366 ± 25
REF-17	229.723	−1.609	80.4884 ± 0.0002	721.3438 ± 0.0002	−7.92 ± 0.28	−5.72 ± 0.27	0.30 ± 0.02	3376 ± 264

Notes.
[a] Predicted coordinates for equinox J2000.0.
[b] Coordinates in the reference frame of the constrained plate (set 8, with roll = 264.°174).

constants, which are constrained to an arbitrary frame adopted as the reference (the constrained plate). The astrometric model also accounts for the time-dependent movements of each star, given by the absolute parallax $\pi_{\rm abs}$ and the proper motion components, and μ_α and μ_δ, where the indices specify the direction in equatorial coordinates. Therefore, the model is given by the standard coordinates ξ and η:

$$\xi = C_1 x' + C_2 y' + D_1 - P_\alpha \pi_{\rm abs} - \mu_\alpha \Delta t \quad (1)$$

$$\eta = C_3 x' + C_4 y' + D_2 - P_\delta \pi_{\rm abs} - \mu_\delta \Delta t, \quad (2)$$

where P_α and P_δ are parallax factors obtained from a Jet Propulsion Laboratory (JPL) Earth orbit predictor (Standish 1990). These are called the equations of condition, which comprises two equations for each star and for each epoch, giving a total of 144 equations to be solved simultaneously. In order to find a global solution, we used a program written in the GAUSSFIT language (Jefferys et al. 1988). Table 5 contains the resulting astrometric catalog.

Van Leeuwen (2007) has recently presented a new reduction of *Hipparcos* data. This resulted in an absolute parallax of HD 136118 $\pi_{\rm abs} = 23.48 \pm 0.54$ mas, which differs significantly from $\pi_{\rm abs} = 19.13 \pm 0.85$ mas, the prior *Hipparcos* determination, and from our *HST* result ($\pi_{\rm abs} = 19.12 \pm 0.22$ mas). When we constrained the parallax in our models to the new higher *Hipparcos* value, we found that the χ^2 of our solution was increased by 20%, which offers evidence that in this case the older *Hipparcos* determination was more accurate, if not more precise.

4. ORBITAL MODEL

4.1. Radial Velocity Model

The velocity we are modeling is the radial component of the stellar orbital movement around the barycenter of the system, which is given by the projection of a Keplerian orbital velocity to observer's line of sight plus a constant velocity Γ. This constant in practice is not the actual velocity of the whole system but a parameter that absorbs all unaccounted for constants. Therefore, we have the following equation:

$$v = \Gamma + K[\cos(f + \omega) + e\cos\omega], \quad (3)$$

where ω is the argument of periastron, e is the eccentricity, K is the velocity semi-amplitude, and f is the true anomaly. The true anomaly contains the time dependence, which is obtained implicitly by solving the Kepler equation:

$$\frac{2\pi}{P}(t - T_0) = E - e\sin E, \quad (4)$$

where T_0 is the epoch of periastron passage, P is the orbital period, and E is the eccentric anomaly, which is related to f by the following equation:

$$\tan\frac{f}{2} = \sqrt{\frac{1+e}{1-e}}\tan\frac{E}{2}. \quad (5)$$

The velocity semi-amplitude can also be written in terms of orbital elements:

$$K = \frac{2\pi}{P}\frac{a_s \sin i}{\sqrt{1-e^2}}, \quad (6)$$

where i is the orbital inclination and a_s is the semimajor axis of the orbit of the star. Using the proportionality between the masses and semimajor axes, $a_b M_b = a_s M_s$, and Kepler's third law, we can rewrite Equation (6):

$$\frac{M_b \sin i}{(M_b + M_s)^{2/3}} = \left(\frac{P}{2\pi G}\right)^{1/3} K\sqrt{1-e^2}. \quad (7)$$

Note that we have introduced the indices s and b to distinguish between stellar and companion's parameters. Equation (7) provides a way to calculate the project minimum mass $M_b \sin i$ of the companion with the assumption that there is a measurement of the stellar mass by other means (e.g., stellar atmospheric models). It is to be noted that this is a lower limit to the mass with the uncertainties mostly dominated by the determination of the stellar mass.

4.2. Apparent Orbit Model

Astrometric data provide positions of the parent star on the plane of the sky at different epochs. The high precision of FGS allows us to measure the apparent orbital movement of the star due to the presence of its companion. Therefore, the astrometric observables to be modeled are the coordinates of the star's apparent orbit.

First, we write the elliptical rectangular coordinates x, y, in the unit orbit, given by

$$x = (\cos E - e) \quad (8)$$

$$y = \sqrt{1-e^2}\sin E, \quad (9)$$

where e is the eccentricity and E is the eccentric anomaly. Remember that E carries the dependence on time through the Kepler equation. The projection of this true orbit onto the plane tangent to the sky gives the coordinates Δx, Δy. This projection can be expressed mathematically by

$$\Delta x = Bx + Gy \quad (10)$$

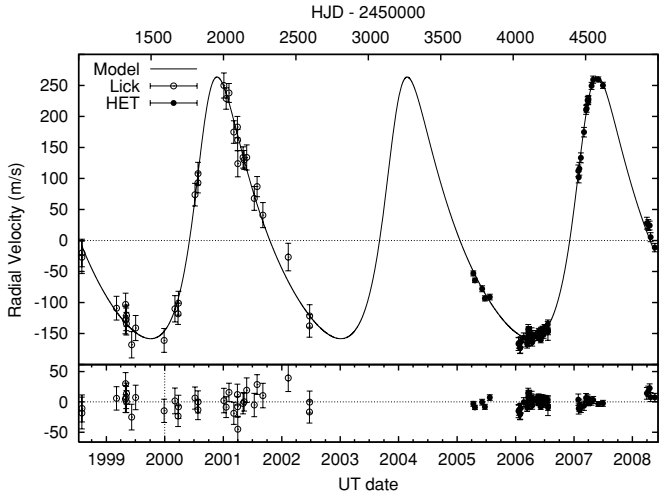

Figure 2. HD 136118 RV HET (filled circles) and Lick (open circles) data, and the best-fit model (solid line).

$$\Delta y = Ax + Fy, \tag{11}$$

where B, A, G, F are the Thiele–Innes constants, given by

$$B = \alpha(\cos\omega \sin\Omega + \sin\omega \cos\Omega \cos i) \tag{12}$$

$$A = \alpha(\cos\omega \cos\Omega - \sin\omega \sin\Omega \cos i) \tag{13}$$

$$G = \alpha(-\sin\omega \sin\Omega + \cos\omega \cos\Omega \cos i) \tag{14}$$

$$F = \alpha(-\sin\omega \cos\Omega - \cos\omega \sin\Omega \cos i), \tag{15}$$

where α is the semimajor axis, Ω is the longitude of the ascending node, i is the inclination of the orbit plane to the plane tangent to the sky, and ω is the argument of periastron. It should be noted that this can be the orbit coordinates for either the parent star or its companion around the barycenter, depending on which semimajor axis is taken; the ω in the respective orbits differ by 180°. We measure the star orbit, so the coordinates of interest are $\Delta x_s, \Delta y_s$, obtained by taking $\alpha = \alpha_s$, which is expressed in miliseconds of arc.

4.3. Combining RV and Astrometry

The orbital elements (P, e, ω, K) in the RV model are the same as the ones used in the astrometric model. However, RV data have a time baseline much longer and a sampling much more abundant than that of the astrometric data. Therefore, in order to obtain the unknown parameters α_s, i, and Ω, we will use the RV parameters to enforce a "constraint relationship" between the astrometric and RV data sets. A way to constrain the orbit without including the time dependence is by making use of Equation (6). Rearranging the terms we have the following equation (Pourbaix & Jorrisen 2000):

$$\alpha_s \sin i = \frac{K P \sqrt{1-e^2}}{2\pi}, \tag{16}$$

where on the left side we have the projection of the semimajor axis of the perturbation orbit. The quantity α_s is an astrometric observable obtained in angular measure. It may be converted to linear measure (AU) by the relation $a[\mathrm{AU}] = \alpha/\pi_{\mathrm{abs}}$. The right-hand side carries all quantities obtained from RV.

If parameters obtained from RV analysis are assumed as constants, there will be three independent measurements, Equations (10), (11), and (16), to determine only three parameters, α_s, i, and Ω. It means that even if one has a poor astrometric coverage of the orbit, it would still converge to a unique solution, although uncertainties in the resulting orbital parameters could be reduced with additional coverage.

The final solution is obtained by performing a simultaneous fit of Equation (3) $[v(P, T, e, \omega, K, \Gamma; t)]$, Equation (10) $[\Delta x_s(P, T, \alpha_s, i, \omega, \Omega; t)]$, and Equation (11) $[\Delta y_s(P, T, \alpha_s, i, \omega, \Omega; t)]$, for RV and astrometry data. Some parameters are constrained via Equation (16) and all parameters are in some way constrained by their physical meaning.

Table 6
HD 136118: RV Orbital Parameters for a One-companion Model

Parameter	HD 136118 b
P (days)	1188.0 ± 2.0
T (JD)	2450614.7 ± 6.3
e	0.34 ± 0.01
ω (°)	317.1 ± 1.3
K (m s^{-1})	210.9 ± 1.6
$M \sin i$ (M_J)	12.00 ± 0.47
Γ_{HET} (m s^{-1})	485.7 ± 1.8
Γ_{Lick1} (m s^{-1})	−1.1 ± 3.8
Γ_{Lick2} (m s^{-1})	−15.3 ± 11.9

Table 7
Statistical Quantities (SQ) for RV Residuals from One-companion Orbit Fit Model

SQ	Lick	HET	All
Mean	−1.21	−0.04	−0.17
Median	0.31	0.73	0.27
σ (m s^{-1})	15.89	8.41	12.03
χ^2	21.29	92.42	117.68
DOF	24	57	88
χ^2_ν	0.89	1.62	1.34

5. RESULTS

All solutions presented below were obtained using GAUSSFIT (Jefferys et al. 1988) programs that minimize χ^2 for the equations shown in the models. As in Section 4.1 above, index b stands for the companion and s for the parent star.

5.1. Radial Velocity Solution

The best-fit model solution yields to orbital parameters shown in Table 6. Figure 2 shows HET RV data plotted together with previously published Lick data (Fischer et al. 2002). The fitted model is also plotted. The residuals are shown in the bottom panel. Table 7 shows the statistical quantities obtained from the residuals, where we used the following terminology—central values: mean and median; standard deviation: σ; sum of squared normalized residuals: χ^2; degrees of freedom: DOF, and reduced chi-square: $\chi^2_\nu = \chi^2/\mathrm{DOF}$. We estimate these quantities for each data set separately and also for all data sets combined together. These allow us to evaluate the legitimacy of the fit.

From Table 7 we note that χ^2_ν for Lick data is close to unity, indicating satisfactory agreement between the dispersion

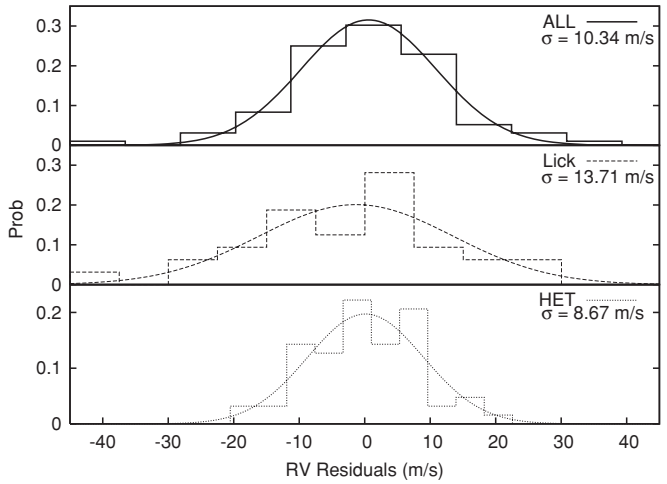

Figure 3. Histogram of residuals from one-companion model for three data sets: all combined (ALL) (top panel), Lick (middle panel), and HET (bottom panel).

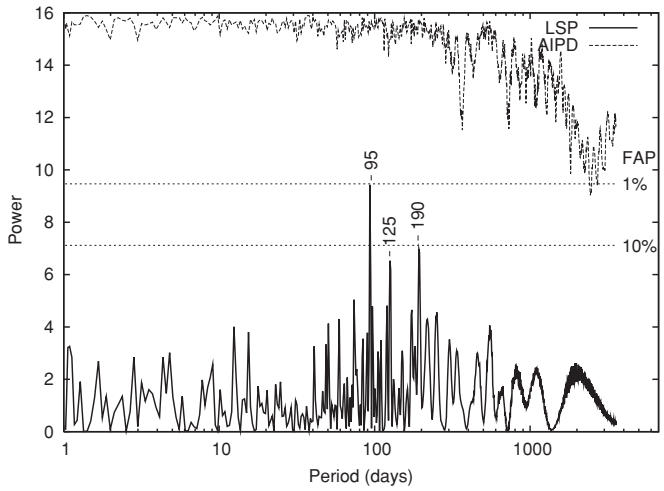

Figure 4. LSP for RV residuals from one-companion model and using all data sets combined (solid line). The thresholds for FAP of 1% and 10% are plotted by dotted lines. Above it the AIPD (see the text) for the same data set is shown (dashed line). The AIPD here is multiplied by a factor of 20 and shifted for the sake of better visualization.

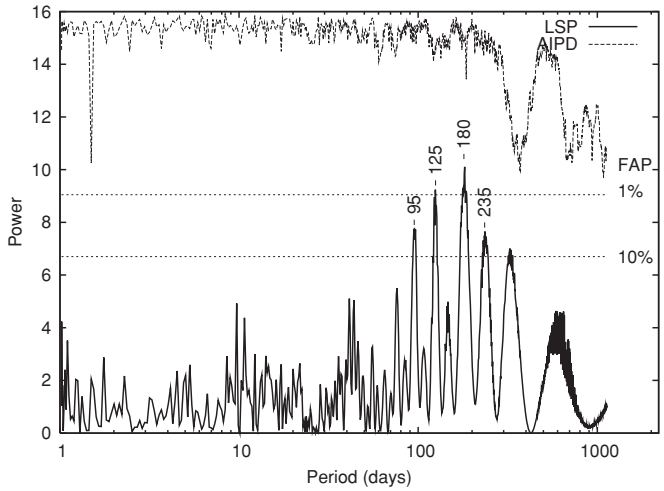

Figure 5. LSP for HET RV residuals from one-companion model (solid line). The thresholds for FAP of 1% and 10% are plotted in dotted lines. Above it the AIPD (see the text) for the same data set (dashed line) is shown. The AIPD here is multiplied by a factor of 20 and shifted for the sake of better visualization.

of residuals and the individual errors. However, this agreement between dispersion and errors is not as definitive for the HET data. We firstly check whether the residuals follow a Gaussian distribution and inspect the errors involved. Figure 3 shows the histogram of distribution of residuals for the two individual data sets separately, Lick and HET, and also for both data sets combined (hereafter "All"). We can see the different dispersion for each data set. We note that each individual data set, either HET or Lick, is not exactly following a normal distribution. We call attention to the fact that the dispersion on HET residuals is about 3 times larger than the error ($\sim$3 m s^{-1}) estimated from previous work (e.g., Bean et al. 2007). This discrepancy may be identified with an unaccounted systematic effect. Below we investigate the detection limits for any further periodic signal that could still be present in our data.

5.2. Limits on Additional Periodic Signals in the RV Data

The customary method for searching periodic signals in unevenly spaced data is by means of the Lomb–Scargle Periodogram (LSP) (Scargle 1982). Figures 4 and 5 show the LSP of residual RV data for two different data sets, respectively: All and HET. The sets are analyzed separately because they have different errors (see Table 6). The power in the LSP is weighted by the overall variance, therefore if one mixes two sets with different variances it would result in an overestimated power for higher levels of noise. The downside of analyzing data sets separately is that sampling becomes different as you have different time coverage and it may affect the detectability for some frequencies.

The LSP for Lick data does not seem to show any expressive power (Fischer et al. 2002). The LSP for HET data set (Figure 5) shows some peaks at the limit where false alarm probability (FAP) is as low as about 1%. The combined data set also shows some power below the level of 1% FAP. This indicates that either there is still an unaccounted periodic signal or the sampling for those frequencies is poor. The latter may be analyzed by the method we describe below.

We introduce a quantity to evaluate how much we can trust some high power found at a given frequency based on sampling for that frequency. We call this quantity the amount of information in the phase diagram (AIPD). It is defined by the following expression:

$$I = -\sum_{i=1}^{N_b} p_i \ln p_i / \ln N_b, \tag{17}$$

where N_b is the number of bins in the phase diagram, p_i is the probability of finding a data point within a given bin i, and may be calculated by $p_i = n_i/N$, where n_i is the number of points inside the bin i and N is the total number of data points. Note that the dependence on the period arises from the construction of the phase diagram. This quantity is normalized and therefore it varies from 0 to 1. When $I = 0$ it means that all data points are found within a single bin in the phase diagram and hence sampling for that frequency is very poor. On the other hand, when $I = 1$ it means that probability p_i is the same for every bin and data are equally distributed along all bins. This gives you an ideal coverage of the phase diagram. We call attention to the fact that AIPD does not measure the statistical significance of the number of data points but only the significance of how well

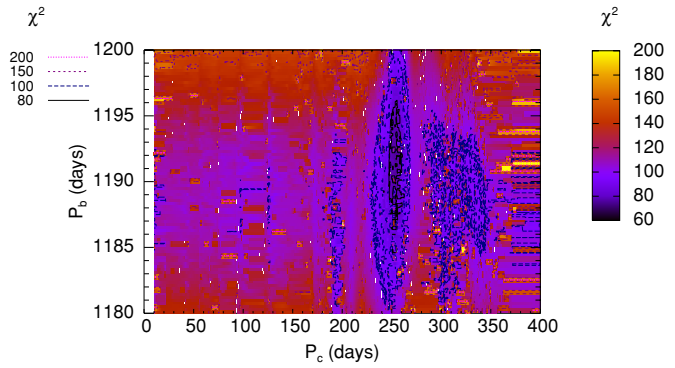

Figure 6. χ^2 map from a two-companion fit model for HET and Lick data. The grid resolution is about 0.3 day (1100 × 90 points). Contour lines show four different levels of χ^2. The best-fit solution has the lowest value at $\chi^2 = 76.6$.
(A color version of this figure is available in the online journal.)

these points are distributed in the phase diagram. Therefore, an issue of concern is the choice of an adequate N_b. We suggest the choice is made in the same fashion as when you build a traditional histogram for inspecting probability distributions. Our choice of N_b is that of $N/N_b > 30$ data points per bin. If N is small enough to make $N_b < 10$ then we assume $N_b = 10$.

Figures 4 and 5 also show a plot of AIPD (in the plot it is multiplied by 20 and shifted for the sake of visualization). We note that some of the high-power periods in the LSP also present a decreasing on the AIPD, which means a deficit of sampling for those periods. This is evident for the one-year period where there is always a lack of data for some part of the phase diagram. If you fold the one-year phase diagram twice there will still be some lack of data coming from the one-year sampling problem. This can be seen from the smaller decreases at the half-year period. Although it is smaller it may still affect the LSP. If one disregards the powers at periods which are close integer fractions of a year there will be no significant power left on the LSPs.

However, the existence of an additional signal cannot be ruled out by looking only at the LSP for the following reason. If the signal comes from an orbit which follows the RV model (Equation (3)), then it may be considered solutions for eccentric orbits instead of strict sine and cosines as in the LSP. An alternative periodogram using the orbit solution is explored in Gregory (2007). We propose a strategy to find a possible hidden signal in our particular case, although it could be expanded and applied for any other system.

Our strategy consists in making multiple attempts to model the RV, using a two-companion model (linear superposition of two Keplerian orbits), and keeping the trial periods as constants in the fitting process. This process forces the minimization algorithm to search for the best solutions for each chosen period. This approach could result in a lower χ^2 when including a hidden periodic component. Figure 6 shows a χ^2 map over a range of periods for a two-companion model fitting RV HET and Lick data simultaneously. The grid point resolution is 1100×90, which means a step on the trial periods of about ∼0.3 day for both components. From Figure 6, we can see a region around 255 days where we found an island of lower χ^2 (darker regions), which indicates the presence of an additional signal. We note that the relatively high power peak at ∼95 days in the LSP (see Figure 4) is now ruled out, because any attempt of fitting a secondary orbit with this period results in larger χ^2. This approach does not prove the existence of another companion in the system. Rather it shows an effective way of finding solutions

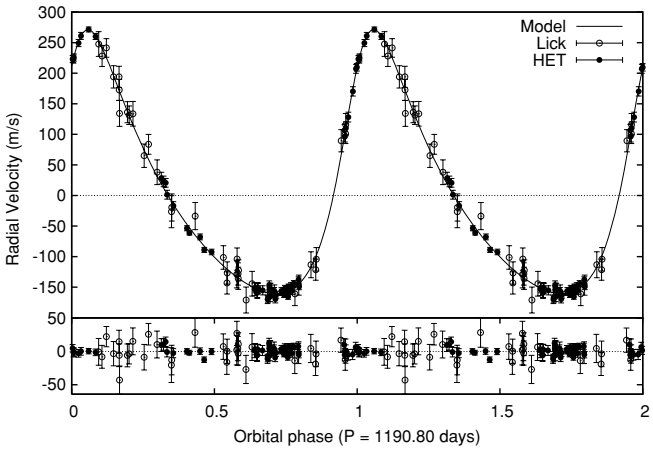

Figure 7. Phase diagram folded with period 1190.8 days. RV HET (filled circles) and Lick (open circles) data subtracted the "nuisance orbit" model. The solid line shows the best-fit HD 136118 b orbit model. Residuals from the two-companion model are plotted in the bottom panel.

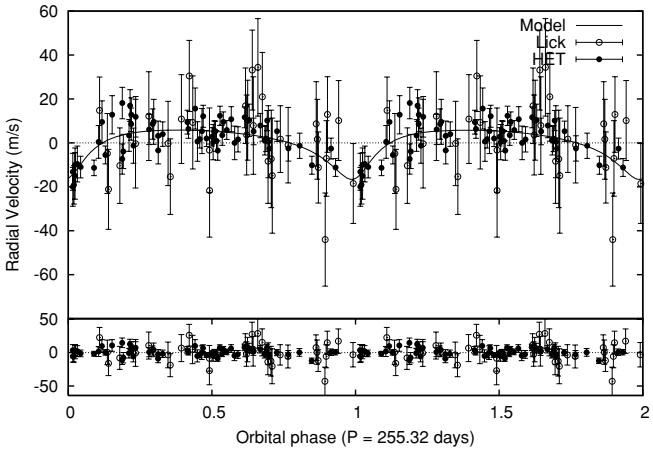

Figure 8. RV HET (filled circles) and Lick (open circles) residuals from HD 131168 b orbit model and the best-fit "nuisance orbit" model plotted in the phase diagram folded with period 255.32 days. Residuals from the two-companion model are plotted in the bottom panel.

that are considerably improved by adding a weak periodic signal that could not be detected in the LSP. Moreover, our model uses Keplerian orbits, which look not only for a periodic signal but for a signal with the shape of an orbit.

Then, we performed a refined fit using the Levemberg–Marquardt method and then a robust fit method for a two-companion model with an additional signal with a period of about 255 days. This solution presents a notable improvement on the minimization of χ^2 if compared to the one-companion model (see Tables 7 and 8). The parameters for a two-companion model are shown in Table 9. From Table 8, we note an improvement on all statistical quantities. The σ dispersion for HET data is now in agreement with that we expected. Figures 7 and 8 show the phase diagram of RV data and the respective component orbit model.

Such a solution suggests the presence of an additional lower mass companion to the system. However, this would be a very eccentric orbit and a considerably large $M \sin i$ planet, which makes us believe that such a body could hardly coexist with a brown dwarf orbiting the same system at the distances they seem to be. In fact, we have performed a stability analysis using the MERCURY package (Chambers 1999). We have input the two companions around HD 136118, and considered the minimum

Table 8
Statistical Quantities (SQ) for RV Residuals from Two-companion Orbit Fit Model

SQ	Lick	HET	All
Mean	−0.61	0.62	0.34
Median	−1.38	0.31	0.15
σ (m s^{-1})	15.4	5.6	10.3
χ^2	19.9	54.2	76.6
DOF	19	52	83
χ^2_ν	1.05	1.04	0.92

Table 9
HD 136118: RV Orbital Parameters for a Two-companion Model

Parameter	HD 136118 b	Nuisance Orbit
P (days)	1191 ± 1.7	255.3 ± 1.6
T (JD)	2450611 ± 5	2453761 ± 7
K (m s^{-1})	215.8 ± 1.3	11.2 ± 1.9
e	0.353 ± 0.008	0.50 ± 0.11
ω (°)	316.4 ± 0.9	198 ± 16
$M \sin i$ (M_J)	12.23 ± 0.47	0.35 ± 0.07
$a \sin i$ (AU)	2.35 ± 0.16	0.85 ± 0.25
$\Gamma_{\rm HET}$ (m s^{-1})	485.5 ± 1.1	
$\Gamma_{\rm Lick1}$ (m s^{-1})	−1.4 ± 3.3	
$\Gamma_{\rm Lick2}$ (m s^{-1})	−11.4 ± 9.7	

mass, which minimizes interactions. We also explored the full range of inclinations for the second component. The system always becomes unstable for very short time scales. Besides the stability constraint, this detection is at the limit of our instrument, and also if we look at Figure 8 we note that only a few data points are contributing to form the orbit we have obtained. For these reasons, we prefer to be cautious and take this as a "nuisance orbit" to fix an unknown source of systematic error present in the HET data, although the possibility of a second companion is not out of the question. Further re-reductions and observations will be done soon to investigate the origin of this signal. The parameters adopted in the following sections are those from a two-companion model. The modeling of the second component in the RV has a very marginal effect on the parameters of the astrometric detection, so it is not "polluting" our result.

5.3. Simultaneous RV and Astrometry Solution

The system parameters obtained in Section 5 from RV analysis are initially adopted as constants as we search for orbital solutions in the astrometric data. Once close to the solution we free all parameters and obtain the best-fit model for astrometry and radial velocity simultaneously. We obtain a semimajor axis of the perturbation orbit $\alpha_s = 1.45 \pm 0.25$ mas, an inclination $i = 163.^\circ1 \pm 3.^\circ0$, and a longitude of the ascending node $\Omega = 285^\circ \pm 10^\circ$. Figure 9 shows the reduced star positions Δx_s and Δy_s versus time for HD 136118. Although our solutions were obtained considering each data point individually, in Figure 9, in order to provide the reader a better visualization to show how the fit works, we also plot normal points which are the median and respective standard deviation of the mean of each clump of data, representing three different epochs. These collapsed points are also shown in Figure 10, where we plotted Δy_s versus Δx_s and the apparent orbit fit model. Figure 11 shows the distribution of astrometric residuals of Δx (left panel) and Δy (right panel) for all reference stars and all data sets. A Gaussian fit model is superposed for comparison. The fit distribution for both Δx and Δy present a maximum consistent with zero, and a FWHM of 0.87 mas and 1.02 mas, respectively.

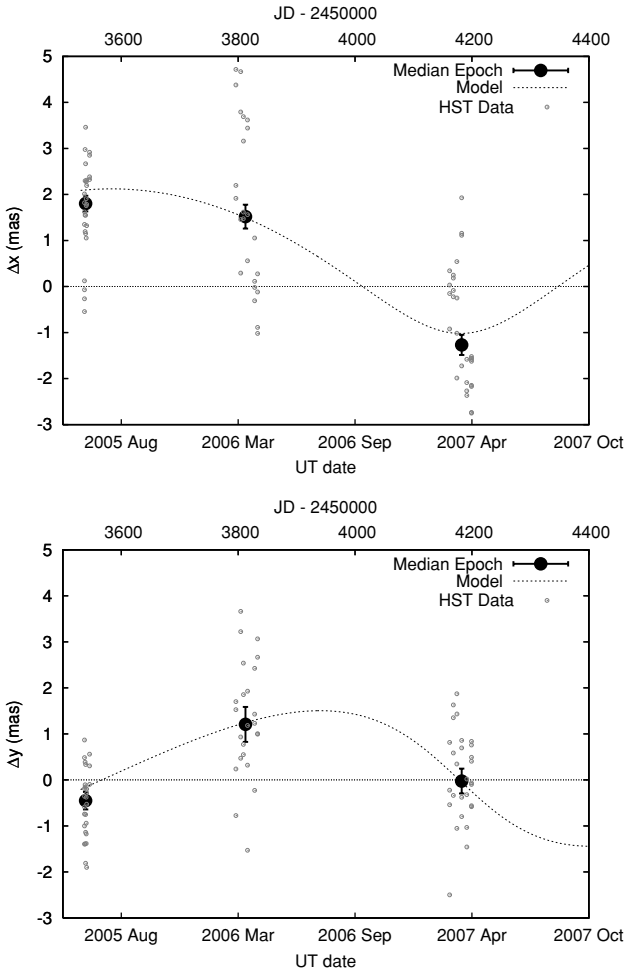

Figure 9. Open circles are the astrometric residuals of HD 136118 in Δx (upper panel) and Δy (bottom panel) versus time. Filled circles with error bars represent three epochs. These were obtained through the median and standard deviation of each grouped data. The perturbation orbit fit model is plotted by dashed lines.

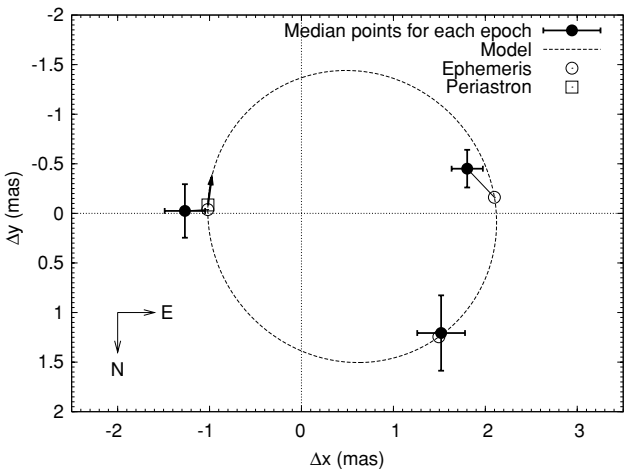

Figure 10. Filled circles with error bars are the median and standard deviation of three groups of astrometric residuals of HD 136118, representing three different epochs. The dashed line is the fit model of the apparent perturbation orbit of HD 136118. Open circles are the positions calculated from the fit model, each of which is connected by a solid line to its respective observed epoch. The open square shows the predicted position of the periastron passage.

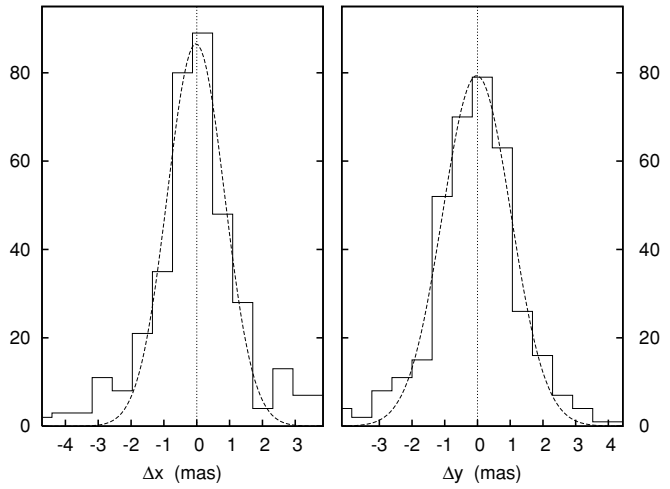

Figure 11. Histogram of Δx (left panel) and Δy (right panel) astrometric residuals for all reference stars. Dashed lines show the fit model for a normal distribution.

Table 10
HD 136118 b Parameters Obtained from Simultaneous RV and Astrometry Solution

Parameter	HD 136118 b
P (days)	1190.9 ± 1.2
T (JD)	2450610.5 ± 3.7
e	0.352 ± 0.006
ω (°)	316.4 ± 0.6
K (m s^{-1})	215.99 ± 0.92
α_s (mas)	1.45 ± 0.25
i (°)	163.1 ± 3.0
Ω (°)	285 ± 10
a_b (AU)	2.36 ± 0.05
M_b[a] (M_J)	42^{+11}_{-18}
M_b[a] ($M_\odot$)	$0.041^{+0.010}_{-0.017}$

Note. [a] It is assumed $M_s = 1.24 \pm 0.07\ M_\odot$.

By determining the inclination we are able to remove the previous degeneracy on the mass of the companion. We calculate the actual mass by iterating Equation (7), which yields $M_b = 42^{+11}_{-18}\ M_J$, firmly establishing HD 136118 b as a bloom in the brown dwarf desert. We also obtain the physical semi-major axis of the companion orbit, $a_b = 2.36 \pm 0.05$ AU. A summary containing all HD 136118 b parameters derived from the simultaneous RV and astrometry solution is shown in Table 10.

6. SUMMARY AND DISCUSSION

HD 136118 is a solar type star with a brown dwarf companion. Table 10 shows a summary of all observed orbital elements of the system.

We found that HD 136118 b has an orbital inclination of $i = 163.^\circ1 \pm 3.^\circ0$, nearly perpendicular to the inferred inclination of the stellar spin axis. This misalignment is an intriguing result since conservation of angular momentum would favor alignment between stellar spin and companion orbital axes, assuming both were formed in the same primordial cloud.

HD 136118 b is likely a brown dwarf companion orbiting at 2.36 AU that falls in the driest region of the so-called "brown dwarf desert" (Grether & Lineweaver 2006). They showed that the frequency of companions in the stellar mass range follows a slope with gradient -9.1 ± 2.9, while in the planetary mass region the gradient is 24.1 ± 4.7. These two separate linear fits intersect below the abscissa at $M = 43^{+14}_{-23}\ M_J$. Surprisingly, HD 136118 b mass is $M_b = 43^{+11}_{-18}\ M_J$. Reffert & Quirrenbach (2006) measured astrometric masses for two exoplanet candidates HD 38529 c ($M = 37^{+36}_{-19}\ M_{\rm Jup}$) and HD 168443 c ($M = 34 \pm 12\ M_{\rm Jup}$). Both are likely brown dwarf companions around solar-type stars like HD 136118 b. These objects are important cases for studying the mass function at the brown dwarf mass range.

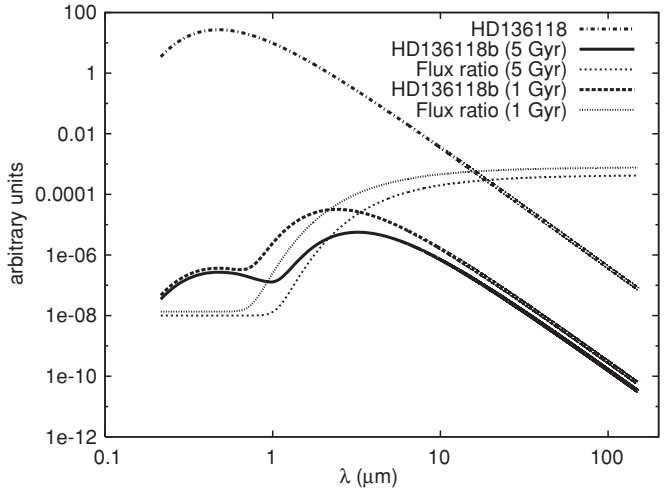

Figure 12. Predicted emission spectrum of HD 136118 (dash-dotted line), emission/reflection spectrum of HD 136118 b, and the flux ratio between the brown dwarf and the parent star for a 5 Gyr and 1 Gyr system age, as indicated in the legend.

According to the evolutionary dusty model for brown dwarfs of Baraffe et al. (2001) and Chabrier et al. (2000), assuming $M_b = 0.041^{+0.010}_{-0.017}\ M_\odot$ and the age of the brown dwarf as 5 Gyr, HD 136118 b has a temperature of about $T_b = 900$ K and a radius of $R_b = 0.086\ R_\odot$. If one considers the uncertainty in the age of the system (see Table 1), this brown dwarf may be much younger; therefore considering the age as 1 Gyr, HD 13118 b has a temperature of about $T_b = 1200$ K and a radius of $R_b = 0.1\ R_\odot$. These characteristics classify HD 136118 b as a T dwarf. Using these values we calculate the emission and reflection spectra, and the flux ratio between the brown dwarf and the parent star as shown in Figure 12. The flux ratio increases toward the far infrared (L, M, and N bands), where it can get as high as 10^{-4}.

The astrometric determination of the mass of a low-mass companion can decisively characterize it as a planet. A good illustration of this fact can be seen from the results of our group for three objects that were previously listed as exoplanet candidates: Gliese 876 b, HD 136118 b, and HD 33636 b. Surprisingly, each object has been found to belong to a different class: a giant planet (Benedict et al. 2002b), a brown dwarf (this paper), and an M dwarf star Bean et al. (2007). These results demonstrate the importance of the application of complementary techniques in observing extrasolar planetary systems.

We thank Mr. Casey Kyte for his assistance with the photometry of HD 136118. This work was supported by the Coordenação de Aperfeiçoamento de Pessoal de Nível Superior (CAPES), Brazil. Support for this work was also provided by NASA through grant GO-10704-10989, and 11210 from the Space Telescope Science Institute, which is operated by AURA, Inc., under NASA contract NAS5-26555. This research is based

partially on observations carried out with the Hobby–Ebberly Telescope at McDonald Observatory. This research has made use of the SIMBAD database, operated at CDS, Strasbourg, France, and NASA's Astrophysics Data System Abstract Service.

Facilities: HET(HRS), *HST*

REFERENCES

Allende Prieto, C., & Lambert, D. L. 1999, A&A, 52, 555
Baraffe, I., et al. 2001, A&A, 382, 563
Bean, J. L., et al. 2007, AJ, 134, 749
Benedict, G. F., et al. 1998, AJ, 116, 429
Benedict, G. F., et al. 1999, AJ, 118, 1086
Benedict, G. F., et al. 2002a, AJ, 123, 473
Benedict, G. F., et al. 2002b, ApJ, 581, L115
Benedict, G. F., et al. 2002c, AJ, 124, 1695
Butler, R. P., et al. 1996, PASP, 108, 550
Butler, R. P., et al. 2006, ApJ, 646, 505
Chabrier, G., et al. 2000, ApJ, 542, 464
Chambers, J. E. 1999, MNRAS, 304, 793
Fischer, D. A., et al. 2002, PASP, 114, 529
Gonzalez, G., & Laws, C. 2007, MNRAS, 378, 1141
Gregory, P. C. 2007, MNRAS, 381, 1607
Grether, D., & Lineweaver, C. H. 2006, AJ, 640, 1051
Henry, G. W., et al. 2000, ApJ, 529, L41
Jefferys, W. H., Fitzpatrick, M. J., & McArthur, B. E. 1988, Celest. Mech., 41, 39
McArthur, B. E., Benedict, G. F., Jefferys, W. H., & Nelan, E. 1997, in The 1997 HST Calibration Workshop, ed. S. Casertano, R. Jedrzejewski, C. D. Keyes, & M. Stevens (Baltimore, MD: STScI), 472
McArthur, B. E., et al. 2001, ApJ, 560, 907
Nelan, E., et al. 2007, Fine Guidance Sensor Handbook, Version 16.0 (Baltimore, MD: STSCcI)
Perryman, M. A. C., et al. 1997, A&A, 323, L49
Pourbaix, D., & Jorrisen, A. 2000, A&A, 145, 161
Reffert, S., & Quirrenbach, A. 2006, A&A, 449, 699
Saar, S. E., & Donahue, R. A. 1997, ApJ, 485, 319
Saffe, C., et al. 2005, RevMexAA, 41, 415
Scargle, J. D. 1982, ApJ, 263, 835
Standish, E. M., Jr. 1990, A&A, 233, 252
Tull, R. G. 1998, Proc. SPIE, 3355, 387
van Leeuwen, F. 2007, A&A, 474, 653
Whipple, A. L., et al. 1995, in Calibrating Hubble Space Telescope: Post-Servicing Mission, ed. A. Koratkar & C. Leitherer (Baltimore, MD: STScI), 119
Zacharias, N., et al. 2004, AJ, 127, 3043